Scientific
Research

Space-Borne Imagery and Geochemical Characters of Post-Orogenic Dyke Swarms, Fatirah-Abu Zawal District, Eastern Desert of Egypt

Ezzat Abdel Rahman, Ashraf Emam

Geology Department, Faculty of Science, Aswan University, Aswan, Egypt
Email: amezzat2010@gmail.com, ashrafemam99@hotmail.com

Abstract

The Precambrian rocks in Wadi Fatirah-Wadi Abu Zawal area, Eastern Desert of Egypt, are cross-cut by numerous post-orogenic dyke swarms. Image processing techniques are applied to the enhanced Thematic Mapper plus (ETM+) data for lithological mapping and spectral characterization of these dyke swarms. Band ratios and principal component analysis (PCA) yield conspicuously effective results. Depending on mineralogical and geochemical data, two petrogenetic groups of dyke swarms have been recognized: the first group (mafic dykes) comprises basalt, basaltic andesite and andesite, while the second group (felsic dykes) corresponds to dacite and rhyolite in composition. The mafic dykes are tholeiitic to calc-alkaline, while the felsic dykes display significant calc-alkaline affinity. The Na_2O, K_2O, Ba, Y, Rb, Zr and Th contents increase from basic to acidic dykes and vice versa relative to CaO, MgO, Fe_2O_3, Sr, V, Co and Ni contents. These dyke swarms have been emplaced in post-collisional, destructive plate margin settings during periods of extension. The basic dykes have characteristics of volcanic arc setting, whereas the acidic dykes display geochemical features of within plate rocks. The chemical differences between the mafic and felsic dyke swarms favor that the two groups of dyke swarms cannot be related to the same magma source, but they are formed from two different parental magmas.

Keywords

Dyke Swarms, Fatirah, ETM+, Band Ratios, PCA, Geochemistry

1. Introduction

The Arabian Nubian Shield (ANS) is a compilation of Neoproterozoic juvenile arcs, younger sedimentary and volcanic basins, voluminous granite intrusions, and enclaves of pre-Neoproterozoic crust that crop out in the western Arabian Plate and the northeastern African Plate at the northern end of the East African Orogen [1]-[3]. Moreover, the final Pan-African phase of igneous activity in the Eastern Desert of Egypt, as a part of the ANS, is characterized by emplacement of bimodal Dokhan volcanics [4], younger granitoids [5], and numerous mafic to felsic dyke swarms [6] [7]. The dykes and dyke swarms are a common feature in the Neoproterozoic ANS terranes [8]. They represent a transitional period from compressional to extensional tectonic setting and their origin is controlled by lithospheric dynamics or passive rifting [6] [7] [9] [10]. In the Eastern Desert and Sinai Peninsula, these dykes are basaltic to rhyolitic in composition, closely associated with granitoids, and intruded under extensional conditions [7] [10]-[12]. The dyke swarms provide a window into the composition and evolution of the sub-continental mantle and hence the tectonic evolution of the overlying continental crust. Also, they may provide some geochronological controls on the later phases of crustal evolution and their orientation can provide information on the regional stress field at the time of emplacement [13]. Composite dykes that are made up of felsic and mafic rocks are abundant in the ANS, in particular in the Eastern Desert and Sinai of Egypt [14]-[16]. These dykes are incorporated in bimodal basalt-rhyolite dyke suites forming dyke warms up to tens of kilometers long. Regarding with El-Sayed [17], three groups of dyke swarms have been distinguished in the Eastern Desert and Sinai: 1) metamorphosed syntectonic dykes (800 - 650 Ma; [18]); 2) unmetamorphosed post-orogenic dykes (591 - 459 Ma; [15] [19]-[23]) and 3) Neogene dykes (30 - 12 Ma; [24] [25]) related to the updoming and opening of the Red Sea Rift system. The first two groups have variable composition ranging from mafic to felsic, whilst the Neogene dykes have the mafic composition. This paper contributes to characterizing the post-orogenic dyke swarms crosscutting the late Precambrian basement rocks at Wadi Fatirah-Wadi Abu Zawal District, Eastern Desert of Egypt (**Figure 1**). The current study has two essential aims. Firstly, it uses the remote sensing analysis of Enhanced Thematic Mapper (ETM+) data (174/42 path/row, acquisition date 09/03/2005) for detailed geological mapping and understanding tectonic setting of the dyke swarms. Band rationing and principal component transformation are the main remote sensing techniques applied to achieve this aim. Secondly, it aims to provide valuable petrological and geochemical data that help in understanding the origin of dyke swarms, their source component(s) and processes involved in magma genesis and evolution.

2. Geologic Setting

The exposed Precambrian rocks along Wadi Fatirah-Wadi Abu Zawal District (**Figure 1**) comprise metavolcanics (oldest), older granitoids, Dokhan volcanics, Hammamat sediments, younger gabbros and younger granites (youngest). Metavolcanics form a NE-SW elongated belt in the western part of study area. They are represented by island arc metavolcanics (=YMV of Stern, [26]) that are characterized by bedding and lamination, and composed mainly of metabasalts, meta-andesites and their equivalent pyroclastics. Older granitoids occupy the eastern and southern parts of the mapped area and cover about 28% of total area. Generally, they are medium to coarse-grained rocks exhibiting low relief, spheroidal and cavernous weathering. Also, they locally possess foliation, particularly along their eastern margin. These rocks intruded through the metavolcanics and in turn they are intruded by the younger gabbros and younger granites. Therefore, older granitoids enclose xenoliths and roof pendants from the metavolvanics and are dissected by alkali feldspar pegmatite veins that are mined for feldspar ores, especially at Wadi El-Urf.

Dokhan volcanics occupy moderate to high relief terrains in the northwestern part of mapped area. They comprise andesites, quartz dacites, porphyritic rhyodacites and rhyolites where the latter two varieties increase in abundance westward. These volcanics are intruded by the younger granites and the felsic varieties are locally intercalated with the Hammamat sediments that occupy the northwestern corner of the mapped area. Hammamat sediments exhibit low to moderate relief and consist of polymictic conglomerates at the base grading upward into greywackes and siltstones. Younger gabbros crop out along Wadi Abu Zawal as homogeneous bodies that form terrains of low to moderate relief. They intruded the metavolcanics and older granitoids, and in turn they are intruded by the younger granites.

Younger granites comprise monzogranites, syenogranites and alkali feldspar granites that are arranged according to their relative age of emplacement. Monzogranites are buff in color and medium to coarse-grained and characterized by low to moderate relief, bouldery weathering and spheroidal exfoliation. They crop out in the
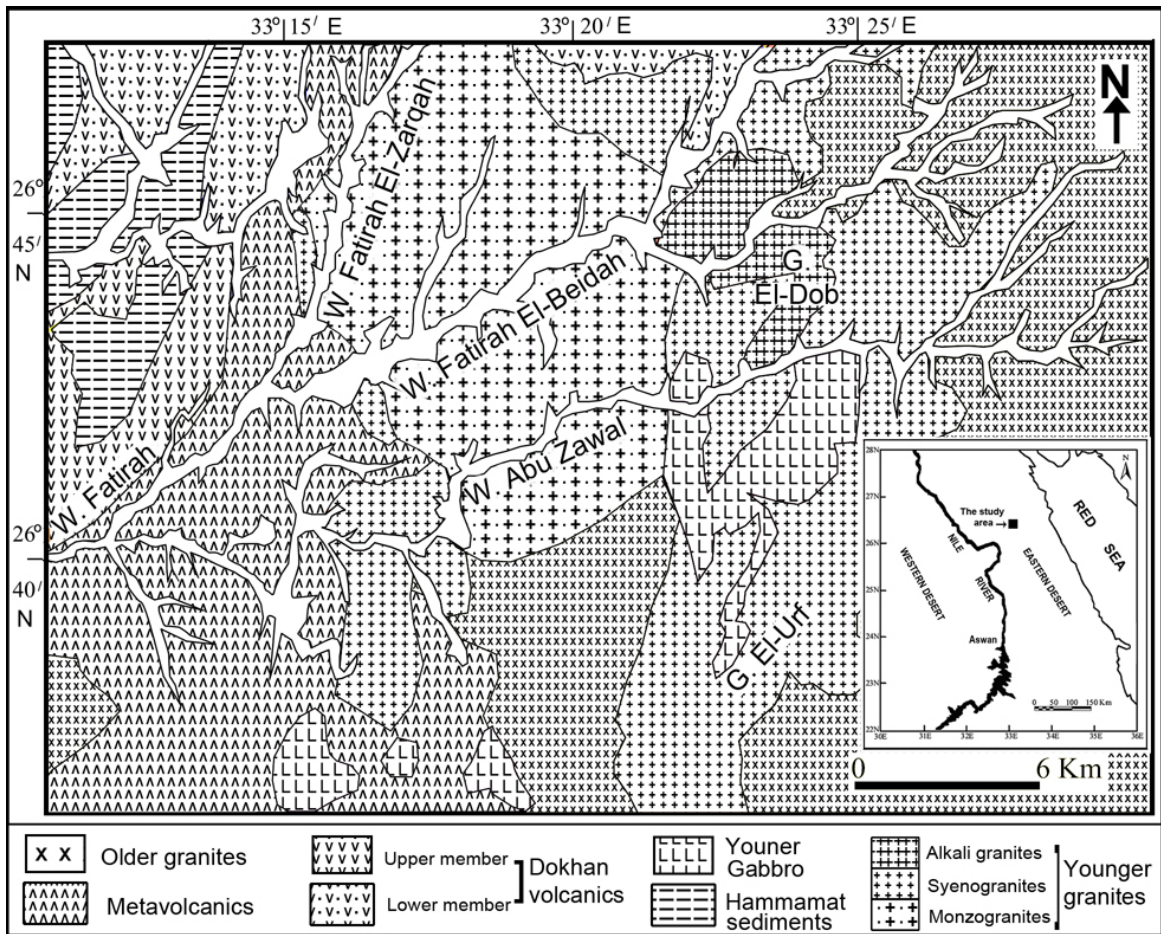
Figure 1. Geological map of Fatirah-Abu Zawal District, Eastern Desert of Egypt.

central part of the area and intruded into the older granitoids and metavolcanics. The contact against the older granitoids is gradational with a hybrid zone, up to 50m wide, whereas its contact with the metavolcanics is sharp and dip away from the granite intrusion. Syenogranites represent the dominant variety among the younger granites in the study area. They are medium- to coarse-grained and pale pink in color. Also, they form elongate bodies with moderate to high relief, intruded into the metavolcanics, older granites and younger gabbros, and consequently enclose xenoliths from the host rocks. Alkali feldspar granites have yellowish pink color and crop out in the northeastern part of the area under consideration. They form small plutons with oval to circular outlines and high relief (e.g. Gabal El-Dob, **Figure 1**).

The exposed Precambrian rocks in the area under consideration are crosscut by numerous post-orogenic dykes of mafic and felsic composition (**Figure 2**). The mafic dykes are the most abundant and widespread in the area comprising three petrographic varieties (basalt, basaltic andesite and andesite). On the other hand, the felsic dykes are petrographically distinguished into dacite and rhyolite. These dyke swarms are unmetamorphosed and arranged as closely parallel sets forming swarms, especially in the central and northern parts of the study area. They have length varying from few hundreds of meters up to 10 km and their width ranges from less than 1m up to 50 m. Also, the dykes are extending in dominant NE, NNE and ENE trends, while some dykes especially in southeastern part of the area exhibit NW trend. Contacts between the felsic and mafic dykes are commonly abrupt, without obvious signs of magma–magma interaction, but also without evidence of chilling. The bimodal dyke suite is the most abundant among the Neoproterozoic dykes in the Eastern Desert of Egypt. Younger granites, gabbros and older granites are the main host rocks of dyke swarms in the central, northern and eastern parts of the study area. Based on field observations and cross-cutting relations of the different dyke swarms, the dykes are straight indicating that they have been apparently emplaced along sharply defined fractures and they are emplaced contemporaneously.
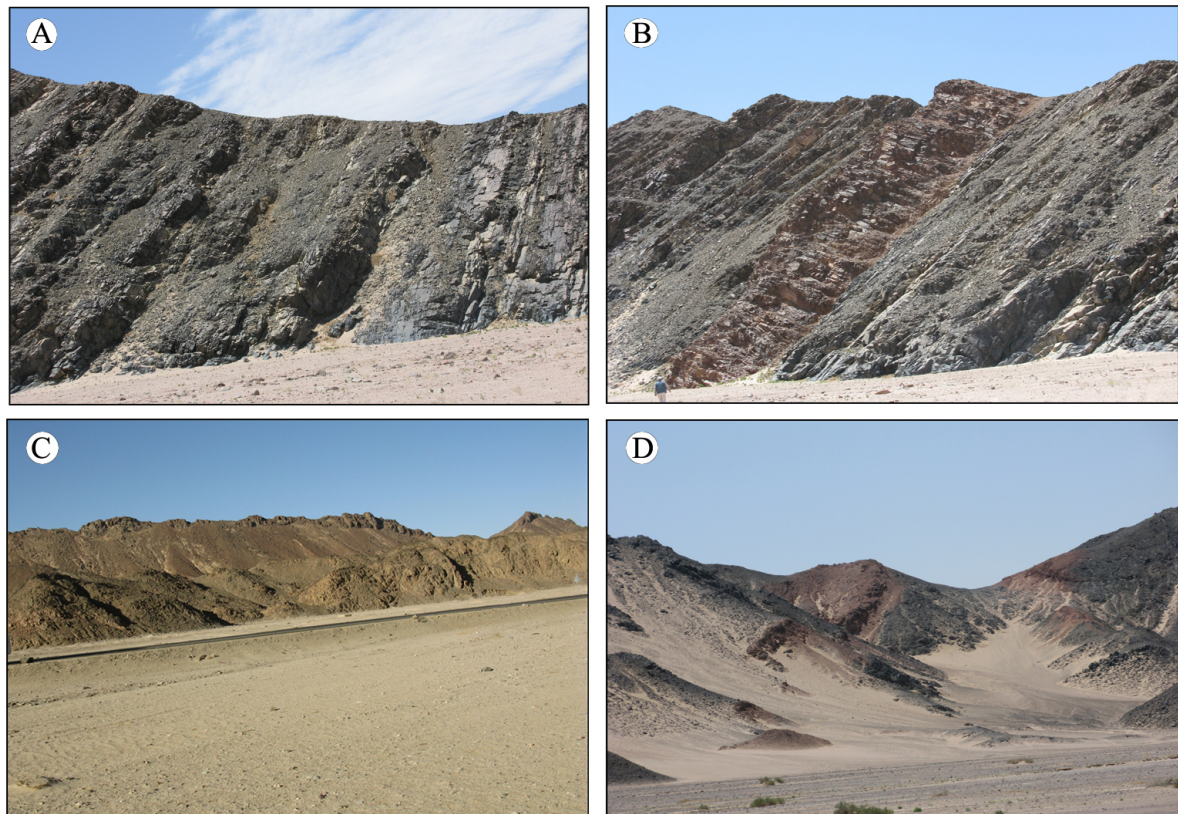
Figure 2. Foliated calc-alkaline metavolcanics are intruded by (A) subparallel basalt to andeite and (B) acidic dyke swarms; (C) Acidic dykes intrude the granitoid rocks; (D) Acidic dyke is cut by basic one and both are intruded into the gabbroic rocks along Wadi Abu Zawal.

3. Petrography

Older Granitoids are Petrographically distinguished into quartz diorites, tonalites and granodiorites that grade imperceptibly into each other. Quartz diorites are medium to coarse-grained and characterized by hypidiomorphic granular texture, with weak foliation. These rocks are composed essentially of plagioclase, quartz, biotite, hornblende and very minor alkali feldspars. Sphene, zircon, apatite and opaques are the main accessories, whereas epidote, chlorite, sericite and kaolinite are secondary minerals. Tonalites are mineralogically and texturally similar to the quartz diorite, but differ in containing higher amounts of quartz. Granodiorites are coarse-grained and massive rocks, characterized by hypidiomorphic granular texture and composed mainly of plagioclase and quartz, together with alkali feldspars, biotite and hornblende. Zircon, apatite, sphene and opaque minerals are accessories, whilst chlorite, sericite and kaolinite are secondary minerals. In all varieties of older granitoids, Quartz fills the interstices between crystals of the early formed minerals, and displays wavy extinction as well as encloses zircon and apatite inclusions. Plagioclase possesses composition with anorthite content as (An20 - 35, An15 - 23, and An12 - 20) in the quartz diorites, tonalites and granodiorites, respectively. It occurs as euhedral to subhedral tabular crystals, commonly zoned with altered core and fresh rim. Its crystals are twinned according to the albite, pericline and albite-carlsbad laws. Orthoclase content exceeds 10% in the granodiorites. It forms subhedral to anhedral tabular and simply twinned crystals. Biotite forms subhedral flakes, occasionally altered to chlorite, strongly pleochroic, and enclose inclusions of quartz, apatite, zircon and sphene.

Younger granitoids in the area under consideration are microscopically differentiated into monzogranites, syenogranites and alkali-feldspar granites. Monzogranites are coarse-grained rocks, exhibit seriate porphyritic texture in the outer parts and equigranular hypidiomorphic texture in the core of intrusion. They are mainly composed of quartz, perthite, plagioclase, hornblende and biotite. Opaques, sphene, apatite and zircon are accessories, whereas sericite, chlorite and epidote are secondary minerals. Syenogranites are leucocratic in color,

medium to coarse-grained and composed mainly of perthite, quartz, plagioclase, biotite and sometimes muscovite. Zircon, apatite and opaques are accessories, whereas secondary minerals include chlorite, sericite and epidote. Alkali feldspar granites are medium to coarse-grained, pinkish in color and essentially composed of orthoclase perthite, quartz, riebeckite, biotite and minor amounts of albite. Zircon, fluorite, cassiterite, apatite, allanite and opaques are accessories, whereas cholrite and sericite are secondary minerals. Alkali feldspars form subhedral tabular crystals and are represented by orthoclase perthites in both monzogranites and alkali feldspar granites. In syenogranites, alkali feldspars present as orthoclase and microcline perthites. Generally, perthites are of flame, string and patchy types. Plagioclase has composition with anorthite content as (An14 - 20, An12 - 15, and An5 - 10) in the monzo-syeno- and alkali feldspar granites, respectively. Mica minerals in the studied younger granites are biotite and muscovite. Biotite occurs as anhedral to subhedral flakes that enclose fine zircon prisms. On the other hand, muscovite is recorded only in syenogranites, forming subhedral flakes and scaly aggregates. Hornblende is present only in the monzogranites and forms subhedral to euhedral prismatic crystals with apatite and zircon inclusions. Riebeckite is observed only in the alkali feldspar granites, as anhedral to subhedral crystals, strongly pleochroic from green to bluish green and enclose zircon, opaques and allanite inclusions.

3.1. Mafic Dykes

Basalt and basaltic andesite dykes are the most predominant rock varieties among the studied mafic dyke swarms. In hand-specimens, the mafic dykes are massive fine-grained, and display different color which varies from black to grayish green and greenish grey. Basalts and basaltic andesite dykes are composed mainly of plagioclase (labradorite composition (An55 - 65), augite and hornblende. Chlorite and actinolite are secondary minerals, while opaque oxides are accessories. They are characterized by ophitic to subophitic textures, besides porphyritic and intergranular textures. Plagioclase occurs either as tabular and prismatic phenocrysts (up to 3.8 × 2.7 mm) or as fine-grained subhedral laths (up to 1.4 mm long) in the groundmass. Euhedral to subhedral tabular plagioclase phenocrysts display lamellar twinning and and sometimes zoning with slightly altrered core and fresh rim. Pyroxene is represented mainly by augite which in turn occurs in the form of euhedral to subhedral prismatic phenocrysts and as granular aggregates in the groundmass. Augite is slightly altered to actinolite and chlorite along the crystal margins and cleavage planes.

Andesite dykes are less abundance compared to the basalt and the basaltic andesite dyke swarms. Megascopically, they are fine-grained, massive and display darkgrey to green color. It is commonly aphyric to faithfully porphyritic textures. In thin section, andesite dykes are composed mainly of plagioclase, and few hornblende phenocrysts, embedded in fine grained groundmass consists of plagioclase laths, chlorite, opaque oxides, calcite and saussurite. Porphyritic and amygdaloidal textures are present, where the amygdales are frequently filled with calcite and/or cryptocrystalline silica. Plagioclase (An25 - 45) is slightly altered to sericite and/or epidote. It occurs as subhedral to anhedral phenocrysts up to 2.5 × 3.8 mm, and as fine-grained subhedral laths that constituting the groundmass. In some slices, plagioclase displays zoning with altered core and fresh rim. Quartz, if present, occurs as anhedral fine-grained crystals in the groundmass.

3.2. Felsic Dykes

Dacite dykes are buff to reddish brown color, fine-grained, massive and exhibit porphyritic and less commonly aphyric textures. They are composed mainly of quartz and plagioclase phenocrysts, embedded in fine grained groundmass formed of plagioclase laths, quartz, and opaques. Accessory minerals are opaques, apatite, and zircon, whereas epidote and chlorite are secondary minerals. Plagioclase (An10 - 18) occurs as euhedral to subhedral prisms (up to 2 × 3.7 mm) and partially altered to epidote. Euhedral to subhedral K-feldspar phenocrysts (up to 2.5 × 3.9 mm) and slightly altered to kaolinite ans sometimes sericite. Quartz occurs as large subhedral phenocrysts and fine-grained crystals filling the interstices between the other constituents.

Rhyolite dykes are pink to buff color, fine-grained and massive. Microscopically, the rhyolite is composed mainly of quartz and orthoclase phenocrysts, plagioclase (An < 10), embedded in cryptocrystalline and glassy groundmass that speckled with quartz, feldspars and opaques. Zircon, and opaques are the accessory minerals, while epidote, chlorite and sericite are the alteration products. K-feldspar is represented by euhedral to subhedral tabular and prismatic phenocrysts as well as small laths in the groundmass. Quartz occurs as subhedral phenocrysts (up to 2.5 mm across) and it is frequently fills the interstices between other minerals. Plagioclase forms

Euhedral to subhedral prismatic phenocrysts (up to 2.6 × 3.8 mm) and exhibit lamellar twinning and sometimes zoning. Plagioclase is slightly altered to sericite and epidote. Generally, rhyolite dykes are characterized by porphyritic, glomeroporphyritic and spherulitic textures.

4. Remote Sensing Data Analysis and Interpretation

Remotely sensed data are important source of information needed to achieve purposes of the geological studies, especially geological mapping, mineral exploration and structural interpretation. Several digital image processing techniques (image enhancement, fusion, rationing, and principal component transformation) were employed for lithological mapping and identifying mineral deposits [27]-[42]. However, there are two important factors that should be taken in consideration during lithological mappings by using remote sensing techniques. First is the localization of increased concentration of minerals relative to the background, and second is the characterization of the mineral assemblages [43]. The present study uses subset of corrected Landsat ETM+ data to discriminate between the different lithologic units, the different dyke varieties and delineate the structural lineaments pattern at the Wadi Fatirah–Wadi Abu Zawal area. Remote sensing techniques including band composites, band ratios and principal component transformation are employed in the present research.

The most useful RGB false color combination (FCC) of ETM+ bands is 7-4-2 which exhibits regional structural lineaments, joints and faults [44]. Consequently, the false color composite band image (7-4-2) was created for the study area (**Figure 3**), where it powerfully separates the dyke swarms from their host rocks. Moreover, this FCC image enhances the drainage pattern and structural lineaments features.

Principal component analysis (PCA) is a multivariate statistical technique that selects uncorrelated linear combinations (eigenvector loadings) of variables in such a way that each successively extracted linear combina-
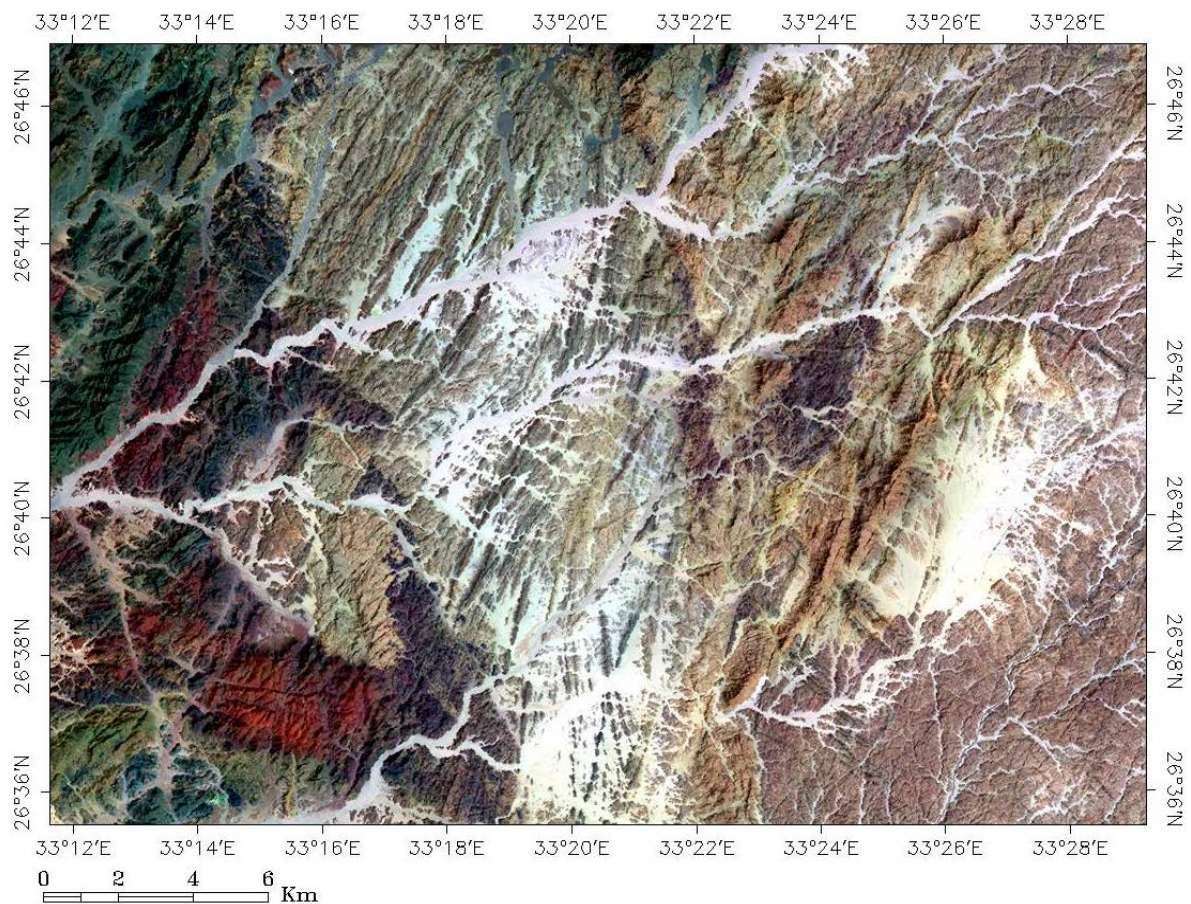
Figure 3. False color composite band image (7-4-2) in RGB mode, enhances the drainage lines, structural lineaments and dyke swarms in Fatirah-Abu Zawal area.

tion, or principal component (PC), has a smaller variance [45]. On the other hand, band rationing of Landsat ETM+ data enhances the spectral differences between bands and reduces the environmental and topographic effects. The band ratio images are prepared simply by dividing the DN values of each pixel in one band by the DN values of another band [46]. Therefore, band ratios have been successfully used for lithological mapping and discriminating between different rock types in the Eastern Desert of Egypt (e.g. [47]-[49]). Also, several studies around the world have used the PCA and band rationing techniques of TM data for mapping hydrothermal alteration zones and lithologies (e.g. [27] [32] [36] [40] [50]-[61]).

The PCA transformation is carried out for the six ETM+ bands (1, 2, 3, 4, 5 and 7) of the study area. Visual examination of the generated FCC PCA images in this study revealed that the RGB combinations (PC3, PC1, PC4) and (PC4, PC2, PC3) are the most informative images. On the hand, (5/7, 4/5, 3/1) and (5/7, 5/1, 5/4 × 3/4) RGB ratio images are the most valuable combinations. Hence, they are used in the present study for discriminating the different varieties of dyke swarms and mapping the different rock units in the study area.

On FCC PCA (PC3:R, PC1:G, PC4:B) image, the dyke swarms can be easily discriminated (**Figure 4**). The mafic dykes have purple image signature whereas the felsic dykes have blue and light blue tone. Dokhan volcanics and alkali-feldspars granites have dark blue and light bluish image signatures, respectively. On contrast, gabbros and basic metavolcanics exhibit pinkish and light purple colors. This FCC is failed to discriminate between monzogranites and syenogranites, where both have greenish color. Also, both gabbros and metavolcanics exhibit the same image signature. Consequently, FCC PCA (PC4: R, PC2:G, PC3:B) image was processed (**Figure 5**) to clearly differentiated between mozogranites (greenish) and syenogranites (dark blue) as well as between gabbros (pinkish) and metavolcanics (light blue).

FCC ratio image (5/7: R, 4/5:G, 3/1:B), discriminates easily between the dyke swarms (**Figure 6**), where the mafic dykes have reddish image signature and the felsic dykes show green and bluish green tone. Dokhan vol-
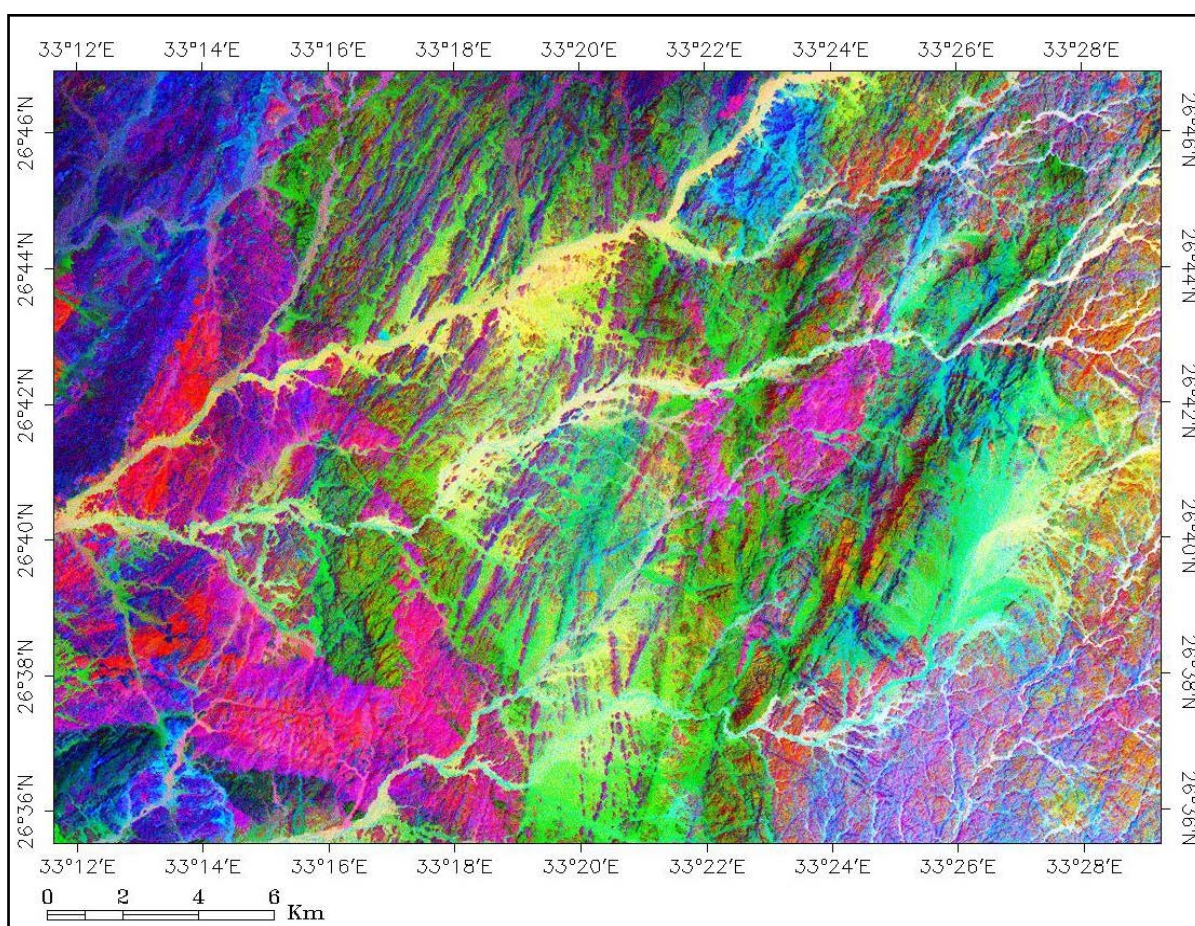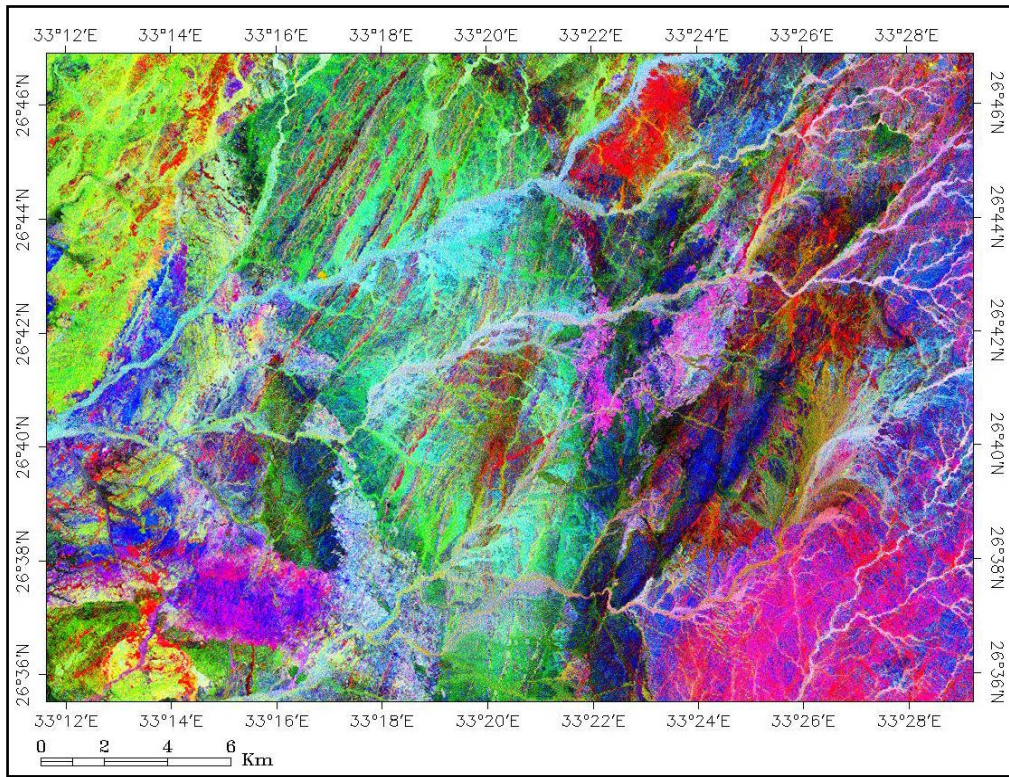

Figure 4. FCC PCA image (PC3, PC1, PC4).
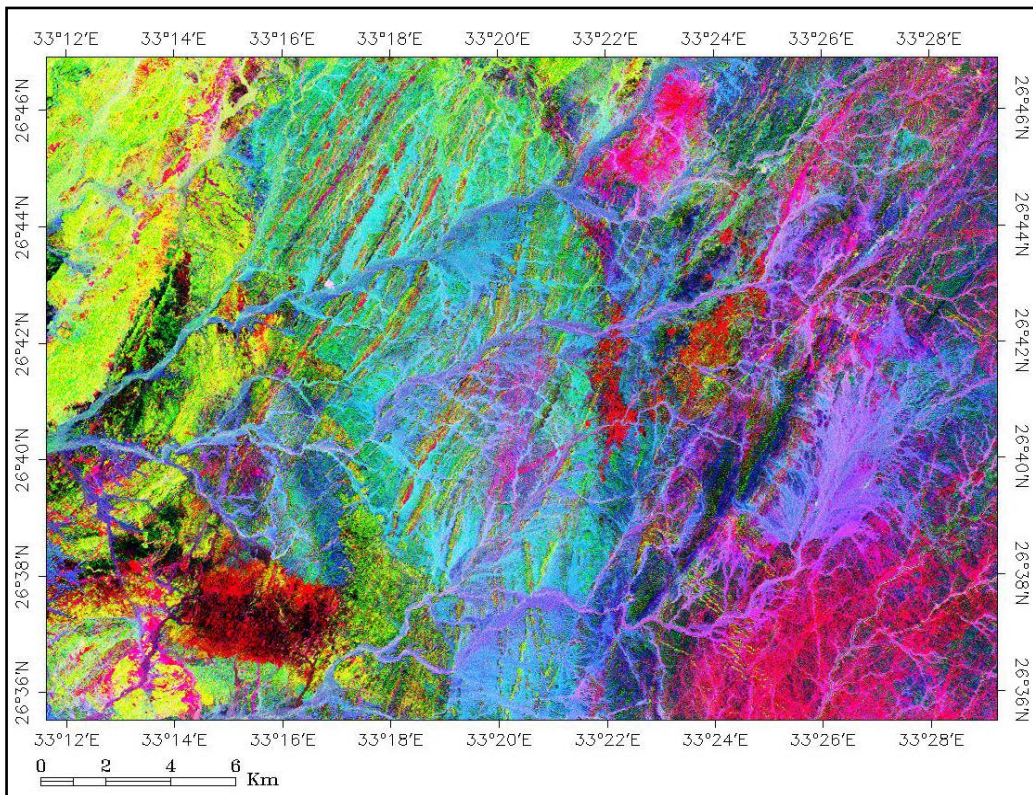
Figure 5. FCC PCA image (PC4, PC2, PC3).

Figure 6. FCC ratio image (5/7, 4/5, 3/1).

canics show lemon color, whereas alkali-feldspars granites have pinkish image signature. On the other hand, gabbros and basic metavolcanics exhibit red and light green colors, respectively. Both monzogranites and syenogranites have light blue image signature. On the FCC (5/7:R, 5/1:G, 5/4 × 3/4:B) image, the mafic dykes have purple image signature whereas the felsic dykes have bluish color (**Figure 7**). Dokhan volcanics and alkali-feldspars granites have reddish and yellowish image signatures, respectively. Gabbros and basic metavolcanics exhibit pinkish and purple colors. Monzogranites and syenogranites have green and light greenish colors, respectively. The FCC (4/2:R, 5/7:G, PC3:B) image was processed to clearly differentiated between the dyke swarms and different rock units occupying the study area (**Figure 8**). The mafic dykes show light bluish color,
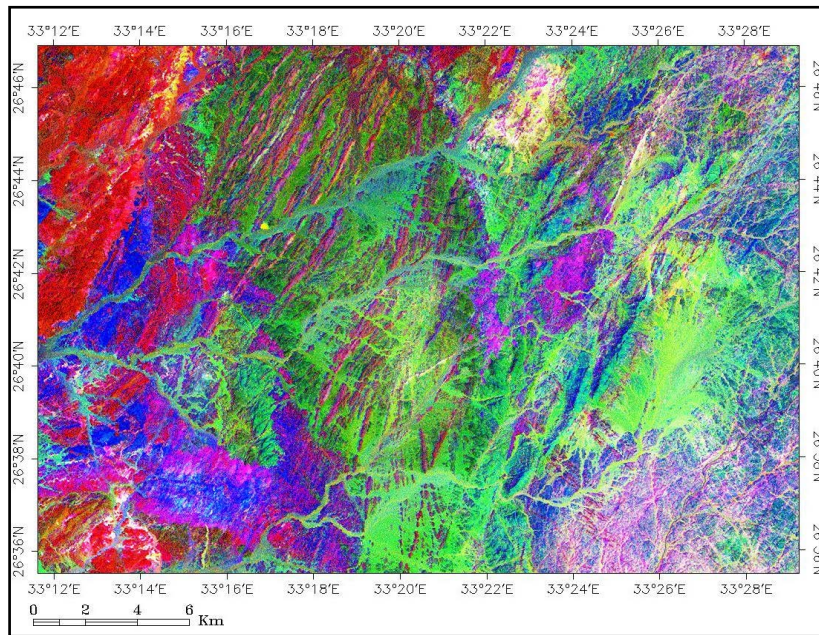

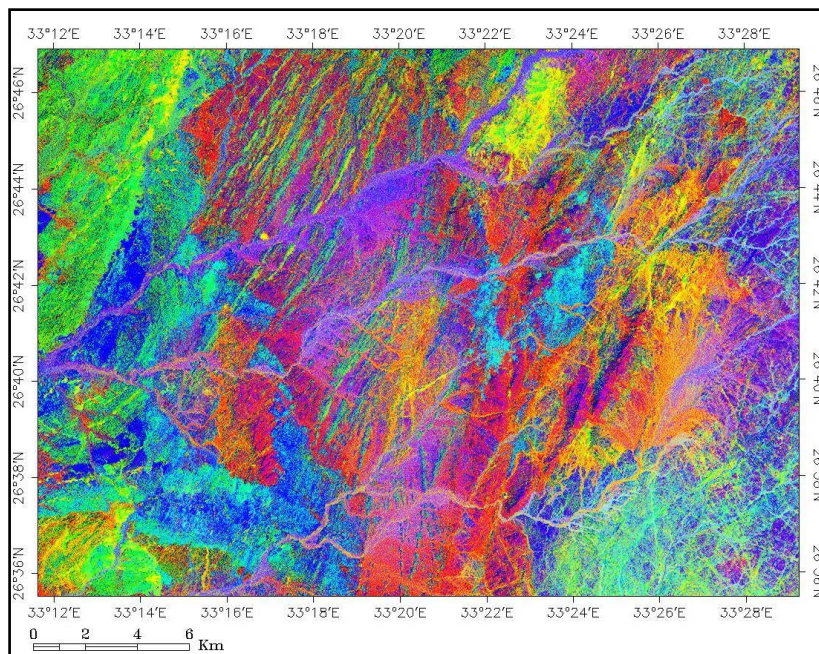**Figure 7.** FCC ratio image (5/7, 5/1, 5/4 × 3/4).

Figure 8. FCC image (4/2, 5/7, PC3) in red, green and blue channels, respectively.

whereas the felsic dykes exhibit orange and reddish colors. Dokhan volcanics have light green color, alkali-feldspars granites have yellowish image signature, while gabbros and basic metavolcanics exhibit light blue and bluish colors. Monzogranites and syenogranites have reddish and orange image signatures, respectively.

5. Geochemistry

5.1. Analytical Techniques

The present study is based on 45 samples collected mainly from the different varieties of dyke swarms in Fatirah-Abu Zawal district, Eastern Desert, Egypt. During the detailed microscopic study for the collected samples, the least altered and weathered samples were selected for major and trace elements analyses. The major and trace elements were determined by using X-ray Fluorescence Spectrometer (XRF) within the Central Laboratories of the Geological Survey of Egypt.

5.2. Major and Trace Element Characteristics

Thirteen representative samples were analyzed (4 samples from basic dykes, 4 samples from andesitic dykes, and 5 samples from acidic dykes) for major and some trace elements. The chemical compositions of representative samples and their CIPW norms are listed in (**Table 1**), moreover some compositional ratios and indices were calculated and listed in (**Table 2**). In the acidic dykes, the SiO_2 content ranges from 73.92% to 77.35%, that of total alkalis ($Na_2O + K_2O$) from 7.48% to 8.97%, CaO from 0.40% to 0.62%, Na_2O/K_2O ratio from 0.63 to 1.23 and $MgO/(FeOt + MgO)$ ratio from 0.06 to 0.15. The andesitic dykes show SiO2 content ranging from 54.1% to 60.62%, ($Na_2O + K_2O$) from 3.14% to 7.26%, CaO from 3.41% to 7.3%, Na_2O/K_2O ratio from 0.62 to 1.57 and $MgO/(FeOt + MgO)$ ratio from 0.27 to 0.46. On the other hand, the basic dykes have SiO2 content ranging from 48.59% to 52.89%, ($Na_2O + K_2O$) from 3.41% to 3.92%, CaO from 5.11% to 7.73%, Na_2O/K_2O ratio from 2.22 to 3.39 and $MgO/(FeOt + MgO)$ ratio from 0.27 to 0.49. It is obvious that the contents of SiO_2, Na_2O, K_2O, Ba, Y, Rb and Th are increased from basic to acidic dykes, and vice versa relative to the contents of CaO, MgO, Fe_2O_3, Sr, V, Co and Ni. Thoronton and Tuttle [62] defined the differentiation index (D.I) as the sum of weight percentage of normative quartz, orthoclase, albite, nepheline, leucite and kasilite. Nocklods (1954) defined the mafic index (M) as $(FeO + Fe_2O_3)*100/(FeO + Fe_2O_3 + MgO)$, while the Mg# index equals [(mol. $Mg \times 100)/(Mg + Fe)$], where each group of rocks are crystallized from magma with distinct Mg# values (De Bari, 1994). The mafic dykes show Mg# values ranging from 42.1 to 65.27, while the acidic dykes have smaller Mg# values (10.54 - 26.1).

The relationship between the different varieties of dyke swarms can be investigated from the variation diagrams of some major and trace elements against the SiO_2 (**Figure 9** and **Figure 10**). The regular variation among the plotted major and trace elements of the basic dyke swarms indicate that the fractional crystallization processes may play significant role in their formation. The CaO, MgO, Fe_2O_3, Sr, V, Co and Ni contents are decreased with increasing SiO_2, while SiO_2, Na_2O, K_2O, Ba, Y, Rb, Zr and Th are increased with increasing SiO_2. This feature is consistent with the crystallization of pyroxene, plagioclase, magnetite and amphibole in the early formed basaltic dykes. Moreover, the increase in the Na_2O, K_2O and SiO_2 reflect the increasing of acidity throughout the acidic dykes. Also, these dyke swarms have mostly low Mg# value indicating that they were produced from highly evolved magma. The $MgO/(MgO+FeO)$ molar ratios (Mg#) for the mafic dykes decrease gradually from basalt through andesite to the most evolved rhyolite. The Na_2O content is generally higher than K_2O in the mafic and felsic dykes.

On the variation diagrams, it is observed that there is a conspicuous compositional SiO_2 gap exists between mafic dykes (basalt and andesite dykes) on the one hand and the felsic dykes on the other hand. Moreover, there is a distinct two trends for the studied dyke swarms one for the mafic dykes and the second for the felsic dykes. Therefore, the presence of a compositional gap and the two trends between them may suggest independent origin (*i.e.* are not comagmatic). Moreover, on these diagrams, the felsic dykes, characterized by low abundance of incompatible elements (**Table 1**), and plots as a separate cluster in almost all covariation diagrams (**Figure 9** and **Figure 10**) and confirmed the observation that they appear not to be related to the mafic dykes via fractionation and suggest that each suite requires different primary melts. Incompatible trace-element variation patterns for the mafic and felsic dykes, normalized to the N-Type MORB [63], are shown in (**Figure 11**). The mafic dykes show an inclined smooth pattern (*i.e.* enrichment in LILE relative to HFSE) and are characterized by

Table 1. Major oxides (%), trace elements (ppm) and CIPW norms of dyke swarms.

Type	Acidic dykes					Intermediate dykes					Basic dykes		
S. No.	1	2	3	4	5	6	7	8	9	10	11	12	13
Major oxides (%)													
SiO_2	77.35	73.92	76.7	74.22	75.6	54.1	55.87	59.37	60.62	49.1	52.71	48.59	52.89
TiO_2	0.17	0.28	0.11	0.16	0.11	1.7	1.29	1.34	1.5	1.34	1.91	3.6	1.54
Al_2O_3	12.11	13.57	11.8	12.97	11.95	12.2	12.87	15.05	14.72	12.89	14.71	12.28	12.32
Fe_2O_3	1.69	1.6	1.01	1.24	1.24	9.3	8.3	7.96	6.92	9.13	12.02	15.41	9.12
MnO	0.01	0.01	0.02	0.01	0.02	0.13	0.01	0.02	0.03	0.02	0.01	0.03	0.01
MgO	0.1	0.16	0.18	0.17	0.14	6.5	7.14	3.22	2.57	8.67	6.65	5.66	7.2
CaO	0.4	0.56	0.62	0.48	0.62	7.3	5.16	5.24	3.41	6.97	5.11	7.28	7.73
Na_2O	4.13	4.31	3.3	4.15	3.96	1.2	2.76	3.74	3.96	2.55	2.68	2.26	2.8
K_2O	3.35	4.42	5.2	4.82	4.11	1.94	1.79	2.38	3.3	0.86	0.79	1.02	1.12
P_2O_5	0.01	0.03	0.01	0.02	0.03	0.42	0.34	0.29	0.47	0.2	0.27	0.95	0.38
L.O.I.	0.62	0.88	0.77	0.93	0.95	3.95	4.07	1	2.15	7.88	2.74	2.54	4.5
Total	99.94	99.74	99.72	99.17	98.73	98.74	99.6	99.61	99.65	99.61	99.6	99.62	99.61
Trace elements (ppm)													
V	18	37	23	31	21	297	290	306	284	323	416	680	361
Cr	13	16	15	15	14	16	41	19	17	695	295	147	354
Co	6	13	9	16	13	35	37	30	22	43	52	55	40
Ni	3	5	1	2	5	14	11	12	15	187	87	70	104
Cu	1	2	1	4	8	35	31	38	21	40	23	15	11
Zn	130	77	143	98	132	105	94	52	71	111	102	120	105
Rb	68	142	89	141	105	38	36	41	62	32	30	23	27
Sr	47	134	67	104	75	395	413	269	254	727	587	661	982
Y	49	32	35	47	38	17	20	13	18	13	12	10	11
Nb	24	25	23	24	23	16	10	11	13	8	6	9	8
Ba	1160	1174	1347	1259	1306	852	948	972	967	286	398	339	245
Yb	2	4	3	1	4	4	6	5	3	9	6	3	4
Hf	9	8	7	7	8	10	6	9	11	7	7	6	8
Ta	2	3	1	2	3	2	3	2	4	1	1	1	2
Pb	13	24	15	23	18	13	19	11	17	11	10	6	3
Th	13	25	12	22	14	5	3	6	9	3	3	3	-
U	3.8	4.1	4.2	4	4.1	3.7	3.7	3.8	3.8	3.9	3.8	3.9	3.7
Zr	218	264	226	261	223	94	187	104	110	58	47	26	22
CIPW norm													
Q	36.10	27.81	33.64	27.97	32.99	13.80	9.67	10.78	12.06	2.83	8.70	6.88	6.30

Continued

C	0.99	0.72	0.00	0.01	0.00	0.00	0.00	0.00	0.00	0.00	0.75	0.00	0.00
Z	0.02	0.02	0.02	0.02	0.02	0.01	0.02	0.01	0.01	0.01	0.00	0.00	0.00
Or	19.90	26.20	31.19	28.83	24.82	11.53	10.44	13.58	19.15	5.15	4.48	5.75	6.53
Ab	37.29	38.83	30.08	37.72	36.34	10.83	24.46	32.43	34.92	23.21	23.10	19.38	24.83
An	2.15	2.84	2.06	2.54	2.75	22.30	17.22	16.66	12.42	21.48	22.87	19.44	17.52
Di	0.00	0.00	1.01	0.00	0.36	9.30	4.91	5.49	1.14	10.00	0.00	7.49	14.57
Hy	1.50	1.44	0.75	1.34	1.17	19.19	22.23	10.62	10.19	25.32	24.93	18.99	17.94
Mt	1.78	1.68	1.07	1.31	1.32	9.78	8.57	8.04	7.10	9.68	12.06	15.38	9.42
Il	0.24	0.39	0.16	0.23	0.16	2.38	1.77	1.80	2.05	1.89	2.55	4.79	2.12
Ap	0.03	0.08	0.03	0.05	0.08	1.00	0.81	0.00	1.13	0.48	0.64	2.26	0.90

Table 2. Compositional ratios and indices calculated for dyke swarms.

Type	Acidic dykes					Intermediate dykes					Basic dykes		
S. No.	1	2	3	4	5	6	7	8	9	10	11	12	13
DI	93.29	92.85	94.91	94.51	94.15	36.16	44.58	56.79	66.13	31.19	36.28	32.02	37.66
Mg#	10.54	16.47	26.01	21.56	18.48	58.06	63.00	44.44	42.37	65.27	52.27	42.10	60.99
ASI	1.09	1.05	0.97	1.00	0.99	0.70	0.81	0.82	0.90	0.72	1.01	0.68	0.62
AI	3.97	4.13	3.27	4.22	4.41	1.28	1.68	1.86	2.34	1.41	1.42	1.40	1.49
M	1.28	1.38	1.43	1.43	1.41	2.82	2.41	2.28	2.01	2.99	2.11	3.42	3.33
MgO/FeOt+MgO	0.06	0.09	0.15	0.12	0.10	0.41	0.46	0.29	0.27	0.49	0.36	0.27	0.44
Na_2O+K_2O	7.48	8.73	8.50	8.97	8.07	3.14	4.55	6.12	7.26	3.41	3.47	3.28	3.92
Na_2O/K_2O	1.23	0.98	0.63	0.86	0.96	0.62	1.54	1.57	1.20	2.97	3.39	2.22	2.50
Ba/Rb	17.06	8.27	15.13	8.93	12.44	22.42	26.33	23.71	15.60	8.94	13.27	14.74	9.07
Rb/Sr	1.45	1.06	1.33	1.36	1.40	0.10	0.09	0.15	0.24	0.04	0.05	0.03	0.03
Zr/Y	4.45	8.25	6.46	5.55	5.87	5.53	9.35	8.00	6.11	4.46	3.92	2.60	2.00
Nb/Y	0.49	0.78	0.66	0.51	0.61	0.94	0.50	0.85	0.72	0.62	0.50	0.90	0.73
Zr/Yb	109.00	66.00	75.33	261.00	55.75	23.50	31.17	20.80	36.67	6.44	7.83	8.67	5.50
Zr/Nb	9.08	10.56	9.83	10.88	9.70	5.88	18.70	9.45	8.46	7.25	7.83	2.89	2.75

negative Zr and Ti anomalies. The felsic dyke samples illustrate similar pattern to the mafic dykes but with higher HFSE contents.

5.3. Chemical Classification and Magma Type

The (Na_2O + K_2O) versus SiO_2 diagram [64] is used to approach the nomenclature of the studied dyke swarms (**Figure 12(a)**). It is obvious that the plotted samples of basic dykes fall within basalt and basaltic andesite fields, those of intermediate dykes fall within basaltic andesite and andesite fields and one sample falls within the trachyandesite field, while those of acidic dykes are plotted within rhyolite field, giving harmony with the petrographic description. This is again supported by plotting the representative samples on the SiO_2 versus $Zr/TiO_2 \times$ 0.001 diagram [65], where the plots of basic, intermediate and acidic dykes fall within sub-alkaline basalt, andesite and rhyolite fields, respectively (**Figure 12(b)**). It is observed that the studied mafic and felsic-
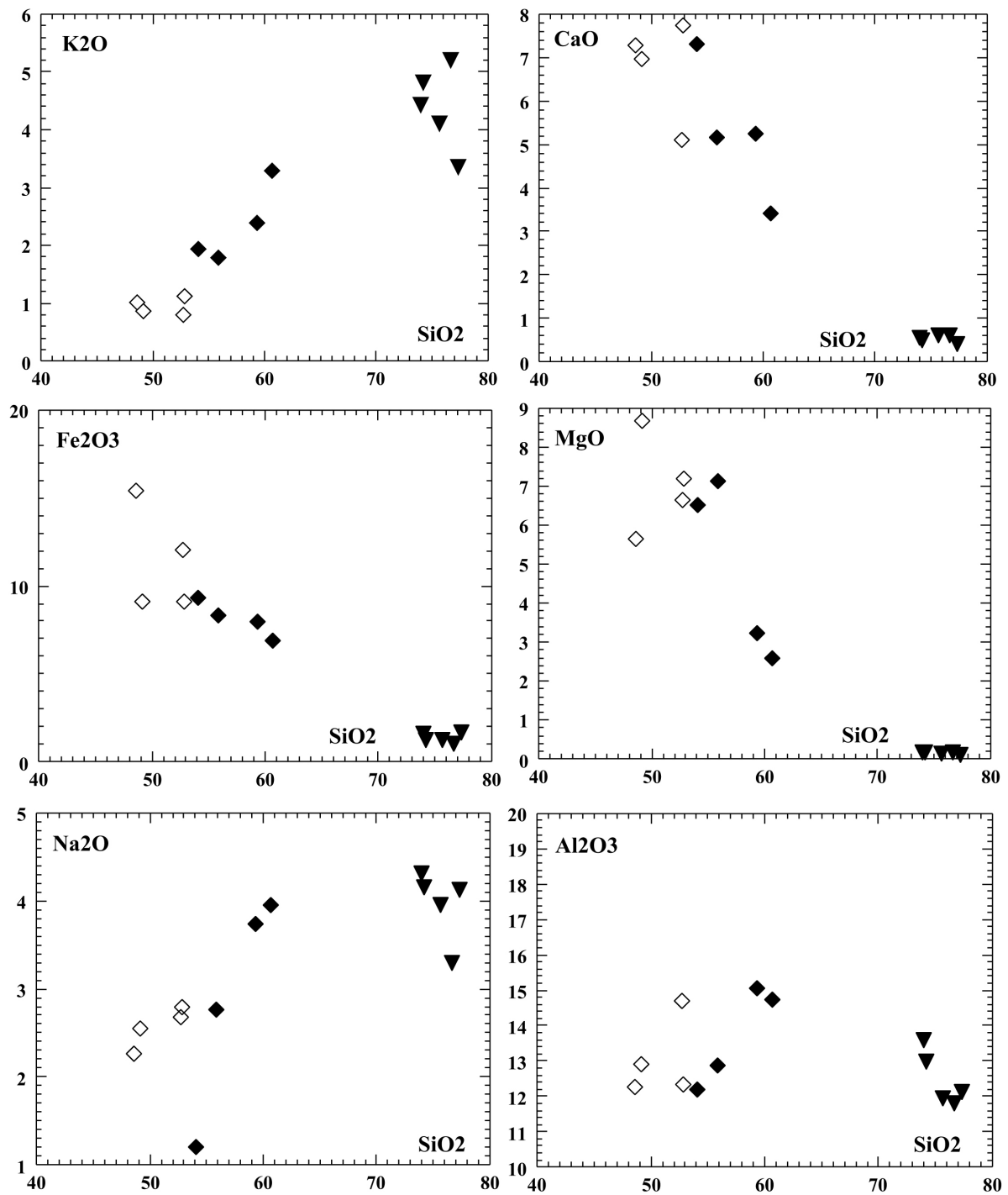
Figure 9. Variation plots of K_2O, CaO, Fe_2O_3, MgO, Al_2O_3 and Na_2O versus SiO_2. Symbols as: ($\diamond$) Basaltic dykes, ($\blacklozenge$) andesitic dykes, ($\blacktriangledown$) acidic dykes.

dyke swarms display a wide compositional range: 1) a mafic dyke swarms (48 - 60 wt% SiO_2) which include basalt, basaltic andesite and andesite and 2) a felsic dyke swarms (73 - 77 wt% SiO_2) that comprising dacite, and rhyolite.

The analyzed samples of dyke swarms have been plotted on the Na_2O+K_2O versus SiO_2 binary diagram [66], where all plots of studied dykes fall within the sub-alkaline field (**Figure 12(c)**). This sub-alkaline nature of
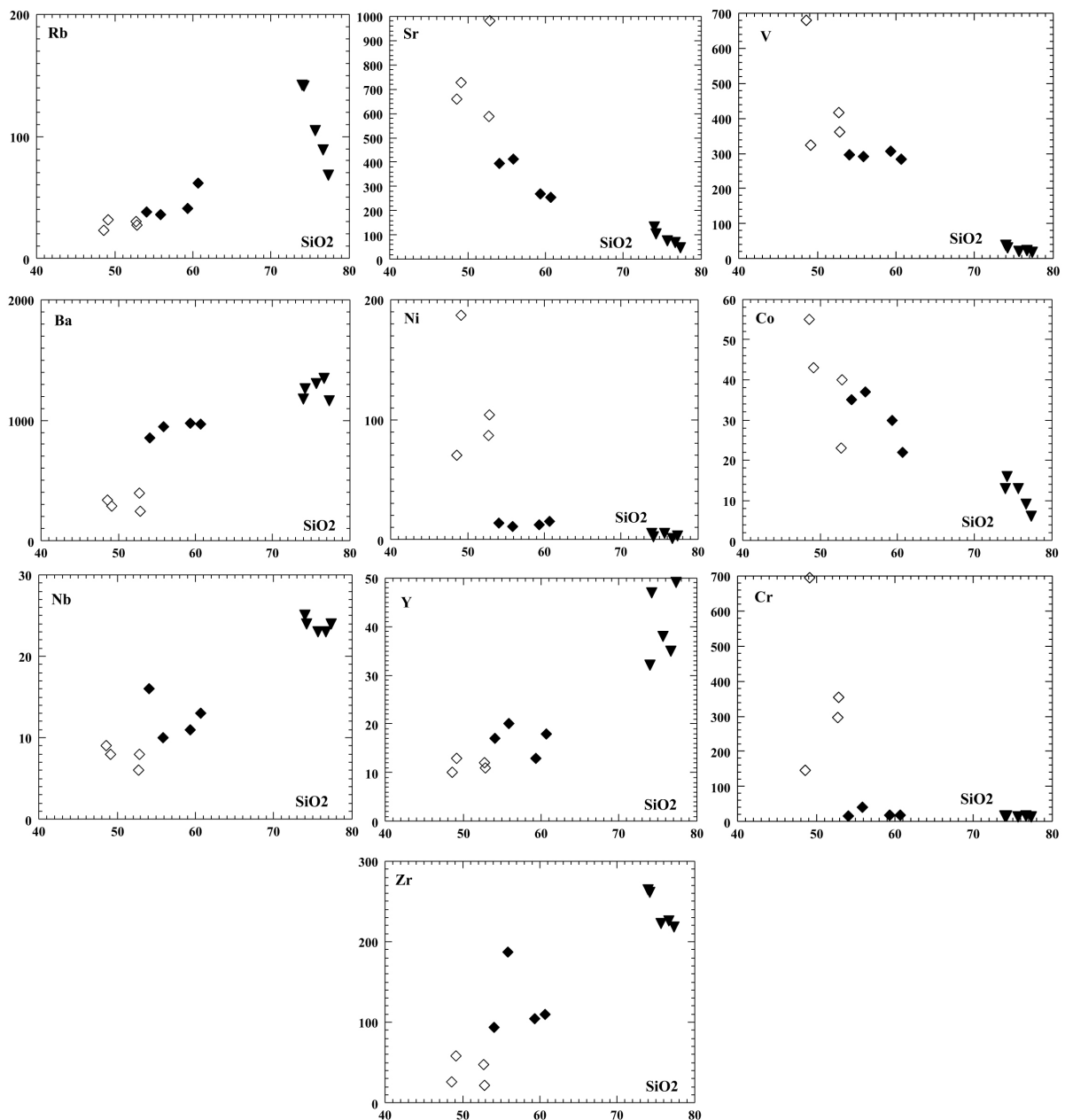
Figure 10. Variation plots of Rb, Sr, V, Ba, Ni, Co, Cr, Nb, Y and Zr versus SiO₂. Symbols as in **Figure 9**.

these dyke swarms may be supported by increase in SiO_2, Na_2O and K_2O, and decrease in MgO/(FeOt+MgO) ratio from the basic to acidic dykes. On the AFM diagram [67], a well-defined tholeiitic to calc-alkaline trend is observed (**Figure 12(d)**). The basic dykes plot away from the MgO apex within tholeiitic field, whereas the andesitic dyke plots mostly fall within calc-alkaline field, except one sample falls within tholeiitic field. On the other hand, all acidic dyke plots fall within calc-alkaline field along the FeOt-total alkalis join in a cluster close to the total alkali apex. This reflects the very low MgO and high alkalis contents in the acidic variety of dyke swarms. Miyashiro [68] suggested that relationship between FeO*/MgO as fractionation index and TiO_2 is diagnostic of tholeiitic and calc-alkaline suites. Therefore, plotting of the analytical data on the TiO_2 versus FeOt/MgO diagram [68] shows that the basic and andesitic dykes follow the tholeiitic trend (**Figure 13(a)**), meanwhile the acidic dykes extends to the calc-alkaline trend, out of diagram limits due to their high FeOt/MgO values. From the above discussion, it is clear that the basic dykes have tholeiitic affinity and the andesitic dykes
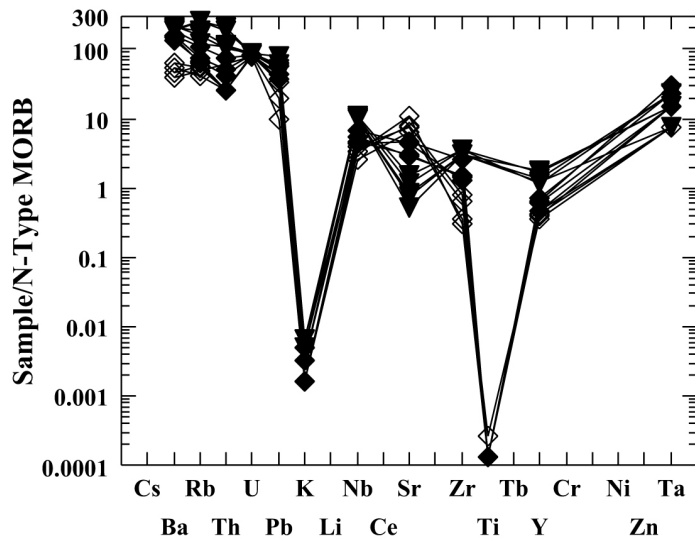
Figure 11. Spider diagram showing the average incompatible elements of studied dyke swarms, normalized to N-Type MORB [63]. Symbols as in **Figure 9**.
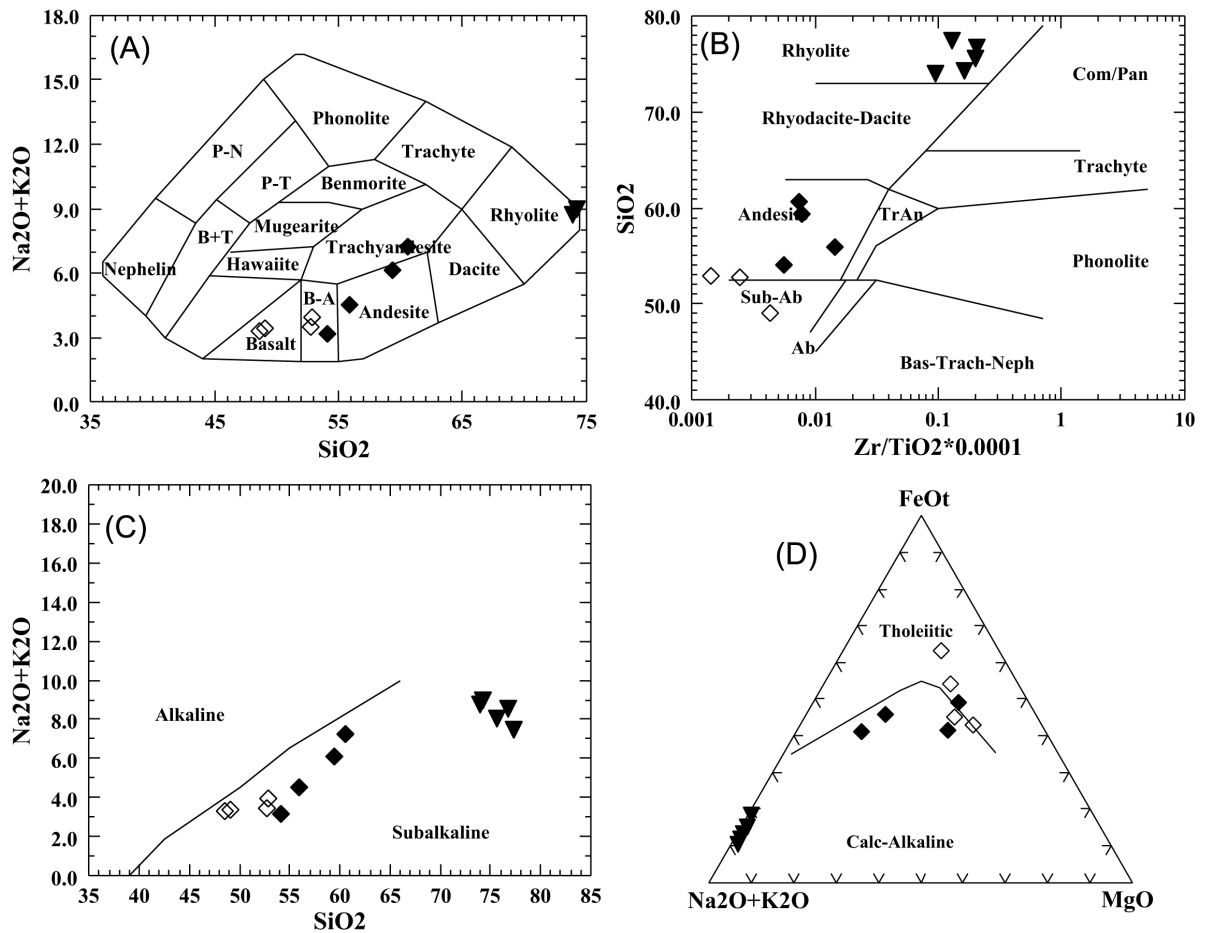

Figure 12. Plots of studied dyke swarms on (A) TAS diagram [64]; (B) Zr/TiO$_2$-SiO$_2$ [65]; (C) Na$_2$O+K$_2$O vs. SiO$_2$ [66] and (D) AFM ternary diagram [67]. Symbols as **Figure 9**.

show tholeiitic to calc-alkaline affinity, while the acidic dykes exhibit calc-alkaline characters.

5.4. Tectonic Setting

The analytical data of dyke swarms are plotted on the Y vs Nb and Y + Nb vs Rb diagrams (**Figure 13(b)** and **Figure 13(c)**) after Pearce et al. [69]. The basic and intermediate dykes fall mostly within the field of volcanic arc environment, whereas the acidic dykes display geochemical features of within plate rocks. On the Th-Nb/16-Hf/3 ternary diagram [70], all plots of dyke swarms fall within the field of destructive plate margin basalts and differentiates (**Figure 13(d)**).

6. Discussion and Conclusion

The Wadi Fatirah-Wadi Abu Zawal District represents the northern most edge of the ANS that formed during the Neoproterozoic (ca.900 - 550 Ma) as part of the East African Orogen by accretion of juvenile arc terrains. The Late Neoproterozoic crustal evolution (ca.610 - 540 Ma) in the ANS occurred in an extensional tectonic environment [7] [71] [72] and was accompanied by abundant igneous activity: emplacement of alkaline granitoids, eruption of bimodal volcanics, and intrusion of bimodal dyke swarms [1] [6] [73]-[75]. In such extensional tectonic environments, ascent of mantle-derived mafic magma into the crust could either melt the existing continental crust and mix with the partial melts or merely result in fractional crystallization of mafic magma leading to granite formation [76]. The plotted samples on the variation diagrams for major and trace elements (**Figure 9** and **Figure 10**) suggest that there are significant geochemical differences between the mafic and felsic dyke swarms. The most effective geochemical differences are the highest content of the mafic dyke swarms in the
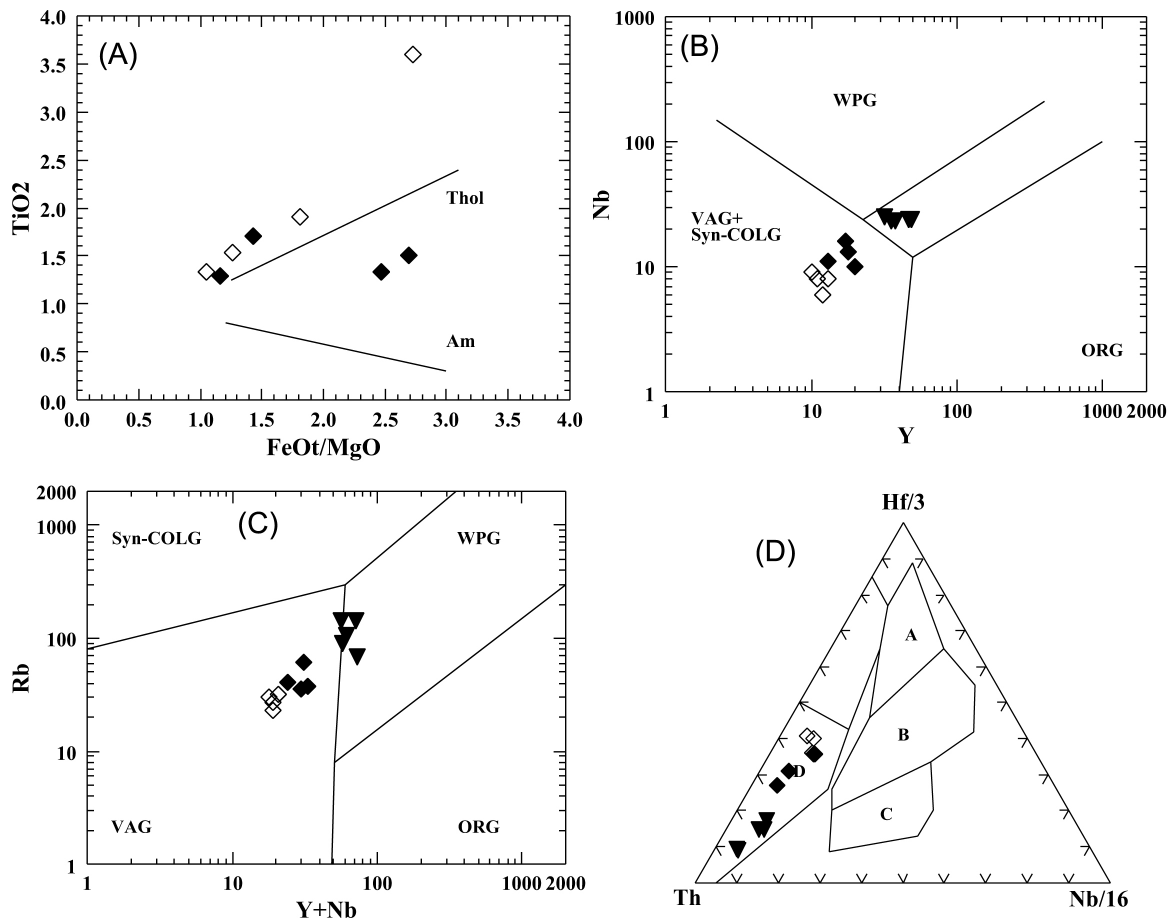

Figure 13. Plots of studied dyke swarms on (A) TiO_2 vs. FeOt/MgO diagram [68]; (B) Y − Nb diagram [69]; (C) Y + Nb vs Rb diagram [69] and (D) Th-Nb/16-Hf/3 ternary diagram [70]. Symbols as **Figure 9**.

HFS elements relative to the felsic dykes. The chemical differences suggest that the mafic and felsic dykes cannot be related and there is no chemical evidence for their generation from the same magma source, as previously argued by Stern and Gottfried [73] for the Eastern Desert dykes. Moreover, the wide variations in the composition of the mafic dykes are attributed to chemical and mineralogical heterogeneities in the mantle sources, differential partial melting of the source materials and modifications of magma composition by fractional crystallization and/or crustal contamination processes. The ratios of Zr/Ti, Zr/Y and Zr/ Nb are not change significantly during the generation of the mafic magma and therefore are very important for evaluation of the relative roles of fractional crystallization, partial melting, and source heterogeneity in producing the variations in magma composition [77] [78]. The presence of negative Ti anomalies for the mafic dykes (**Figure 11**) can have several causes such as amphibole and/or Ti-magnetite fractionation and selective transport in fluids or prior extraction of melts.

7. The Following Are the Main Conclusions

- The dyke swarms of Wadi Fatirah-Wadi Abu Zawal District are differentiated into two petrogenetic groups; namely as mafic and felsic dykes. The mafic dykes comprise basalt, basaltic andesite and andesite, while the felsic dykes are dacite and rhyolite in composition.
- Band rationing and PCA are two effective remote sensing techniques applied on ETM+ data for detailed lithological mapping and spectral discrimination of the dyke swarms of Wadi Fatirah-Wadi Abu Zawal District.
- The RGB (PC3, PC1, PC4) and (PC4, PC2, PC3) PCA images and RGB (5/7, 4/5, 3/1) and (5/7, 5/1, 5/4 × 3/4) ratio images are the most informative images used to clearly discriminate the different varieties of dyke swarms as well as other lithologies in the study area.
- Geochemically, the mafic dyke swarms show tholeiitic to calc-alkaline affinity, with a negative Ti anomaly in their normalized plots of incompatible elements. In contrast, the felsic dyke swarms display significant calc-alkaline affinity. They show decreasing LILE contents and increasing amounts of Y, Nb, and Zr.
- The dyke swarms have been emplaced in destructive plate margin settings during periods of extension. The basic dyke swarms show characteristics of volcanic arc setting, while the acidic dykes display geochemical features of within plate rocks.
- The chemical differences between the mafic and felsic dyke swarms favor that these two types of dyke swarms cannot be related to the same magma source, through fractional crystallization processes, but they have been formed from two different parental magmas.

References

[1]   Stern, R.J. (1994) Arc Assembly and Continental Collision in the Neoproterozoic East African Orogen: Implications for the Consolidation of Gondwanaland. *Annual Reviews of Earth and Planetary Sciences*, **22**, 315-319. http://dx.doi.org/10.1146/annurev.ea.22.050194.001535

[2]   Kusky, T.M., Abdelsalam, M., Stern, R. and Tucker, R. (2003) Preface to Special Issue Precambrian Research on the East African and Related Orogens, and the Assembly of Gondwana. *Precambrian Research*, **123**, 81-85. http://dx.doi.org/10.1016/S0301-9268(03)00062-7

[3]   Johnson, P.R. and Woldehaimanot, B. (2003) Development of the Arabian-Nubian Shield: Perspectives on Accretion and Deformation in the Northern East African Orogen and the Assembly of Gondwana. In: Yoshida, M., Windley, B.F. and Dasgupta, S., Eds., *Proterozoic East Gondwana*: *Supercontinent Assembly and Breakup*: *Geological Society*, Vol. 206, Special Publication, London, 290-325.

[4]   Akaad, MK. and Noweir, A.M. (1980) Geology and Lithostratigraphy of the Arabian Desert Orogenic Belt of Egypt between Lat. 25° 35′ and 26° 30′N. *Bulletin Institute Applied Geology*, *Jeddah*, **4**, 127-134.

[5]   El-Gaby, S. (1975) Petrochemistry and Geochemistry of Some Granites from Egypt. *Neues Jahrbuch für Mineralogie Abhandlungen*, **124**, 147-189.

[6]   Stern, R.J., Gottfried, D. and Hedge, C.E. (1984) Late Precambrian Rifting and Crustal Evolution in the Northeast Desert of Egypt. *Geology*, **12**, 168-172. http://dx.doi.org/10.1130/0091-7613(1984)12<168:LPRACE>2.0.CO;2

[7]   Stern, R.J., Sellers, G. and Gottfried, D. (1988) Bimodal Dyke Swarms in the North Eastern Desert of Egypt: Significance for the Origin of Late Precambrian ''A-Type'' Granites in Northern Afro-Arabia. In: El Gaby, S. and Greiling, R. O., Eds., *The Pan-African Belt of Northeast Africa and Adjacent Areas*, Vieweg, Weisbaden, 147-177.

[8]   Tarney, J. (1992) Geochemistry and Significance of Mafic Dyke Swarms in the Proterozoic. In: Condie, K.C., Ed., *Proterozoic Crustal Evolution*, Elsevier, Amsterdam, 151-179.

[9]   Beyth, M., Stern, R.J., Altherr, R. and Kröner, A. (1994) The Late Precambrian Timna Igneous Complex: Southern Israel: Evidence for Comagmatic-Type Sanukitoid Monzodiorite and Alkali Granite Magma. *Lithos*, **31**, 103-124. http://dx.doi.org/10.1016/0024-4937(94)90003-5

[10] El-Nisr, S.A. and Moghazi, A.M. (2001) Geochemistry, Petrogenesis and Paleotectonic Significance of Dyke Swarms Intruding Neoproterozoic Basement Rocks, South Marsa Alam Area, Eastern Desert, Egypt. *Bulletin of the Faculty of Science*, *Assiut University*, **30**, 117-134.

[11] Friz-Töpfer, A. (1991) Geochemical Characterization of Pan-African Dyke Swarms in Southern Sinai: From Continental Margin to Intraplate Magmatism. *Precambrian Research*, **49**, 281-300. http://dx.doi.org/10.1016/0301-9268(91)90038-C

[12] Beyth, M. and Peltz, S. (1992) Petrology and Major-Element Geochemistry of Dikes at Har Timna, Southern Israel. Geological Survey of Israel, Jerusalem, Rep. No. GSI/13/92, 39 pp.

[13] Worthing, M.A. (2005) Petrology and Geochronology of a Neoproterozoic Dyke Swarm from Marbat, South Oman. *Journal of African Earth Sciences*, **41**, 248-265. http://dx.doi.org/10.1016/j.jafrearsci.2005.04.003

[14] Vogel, T.A. and Wilband, J.T. (1978) Coexisting Acidic and Basic Melts: Geochemistry of a Composite Dike. *The Journal of Geology*, **86**, 353-371. http://dx.doi.org/10.1086/649696

[15] Stern, R.J. and Voegeli, D.A. (1987) Geochemistry, Geochronology, and Petrogenesis of Late Precambrian (~590Ma) Composite Dike from the North Eastern Desert of Egypt. *Geologische Rundschau*, **76**, 325-341. http://dx.doi.org/10.1007/BF01821078

[16] Jarrar, G., Saffarini, G., Baumann, A. and Wachendorf, H. (2004) Origin, Age and Petrogenesis of Neoproterozoic Composite Dikes from the Arabian-Nubian Shield, SW Jordan. *Geological Journal*, **39**, 157-178. http://dx.doi.org/10.1002/gj.950

[17] El-Sayed, M.M. (2006) Geochemistry and Petrogenesis of the Post-Orogenic Bimodal Dyke Swarms in NW Sinai, Egypt: Constraints on the Magmatic-Tectonic Processes during the Late Precambrian. *Chemie der Erde*, *Geochemistry*, **66**, 129-141. http://dx.doi.org/10.1016/j.chemer.2003.12.003

[18] Eyal, Y. and Eyal, M. (1987) Mafic Dyke Swarms in the Arabian-Nubian Shield. *Israel Journal of Earth Sciences*, **36**, 195-211.

[19] Halpern, M. and Tristan, N. (1981) Geochronology of the Arabian-Ubian Shield in Southern Israel and Sinai. *The Journal of Geology*, **89**, 639-648. http://dx.doi.org/10.1086/628627

[20] Stern, R.J. and Manton, W.I. (1987) Age of Feiran Basement Rocks, Sinai: Implications for Late Precambrian Crustal Evolution in the Northern Arabian-Nubian Shield. *Journal of the Geological Society* (*London*), **144**, 569-575. http://dx.doi.org/10.1144/gsjgs.144.4.0569

[21] Abdel-Rahman, A.F.M. and Doig, R. (1987) The Rb-Sr Geochronological Evolution of the Ras Gharib Segment of the Northern Nubian Shield. *Journal of the Geological Society* (*London*), **144**, 577-586. http://dx.doi.org/10.1144/gsjgs.144.4.0577

[22] Moghazi, A.M. (1994) Geochemical and Radiogenic Isotope Studies of Some Basement Rocks at the Kid Area, Southeastern Sinai, Egypt. Ph.D. Thesis, Alexandria University, Alexandria, 377 pp.

[23] Schandelmeier, H., Abdel-Rahman, A.F.M., Wipfler, E., Kuster, D., Utke, A. and Matheis, G. (1994) Late Proterozoic Magmatism in the Nakasib Suture, Red Sea Hills, Sudan. *Journal of the Geological Society* (*London*), **151**, 485-497. http://dx.doi.org/10.1144/gsjgs.151.3.0485

[24] Meneisy, M. (1990) Vulcanicity. In: Said, R., Ed., *The Geology of Egypt*, Balkema, Rotterdam, 157-172.

[25] Camp, V.E. and Roobol, M.J. (1992) Upwelling Asthenosphere beneath Western Arabia and Its Regional Implications. *Journal of Geophysical Research*: *Solid Earth*, **97**, 15255-15271. http://dx.doi.org/10.1029/92JB00943

[26] Stern, R.J. (1981) Petrogenesis and Tectonic Setting of Late Precambrian Ensimatic Volcanic Rocks, Central Eastern Desert of Egypt. *Precambrian Research*, **16**, 195-230. http://dx.doi.org/10.1016/0301-9268(81)90013-9

[27] Abrams, M.J., Brown, D., Lepley, L. and Sadowski, R. (1983) Remote Sensing for Porphyry Copper Deposits in Southern Arizona. *Economic Geology*, **78**, 591-604. http://dx.doi.org/10.2113/gsecongeo.78.4.591

[28] Chavez, P.S. and Kwarteng, A.Y. (1989) Extracting Spectral Contrast in Landsat Thematic Mapper Image Data Using Selective Principal Component Analysis. *Photogrammetric Engineering and Remote Sensing*, **55**, 339-348.

[29] Abrams, M.J. and Hook, S.J. (1995) Simulated Aster Data for Geologic Studies. *IEEE Transactions of Geoscience and Remote Sensing*, **33**, 692-699. http://dx.doi.org/10.1109/36.387584

[30] Rowan, L.C. and Bowers, T.L. (1995) Analysis Of Linear Features Mapped in Landsat Thematic Mapper and Side-

Looking Airborne Radar Images of the Reno 1 Degree by 2 Degree Quadrangles, Nevada and California; Implications for Mineral Resource Studies. *Photogrammetric Engineering & Remote Sensing*, **61**, 749-759.

[31] Sabins, F.F. (1997) Remote Sensing—Principles and Interpretation. 3rd Edtion, W.H. Freeman, New York, 494 pp.

[32] Sabins, F.F. (1999) Remote Sensing for Mineral Exploration. *Ore Geology Reviews*, **14**, 157-183. http://dx.doi.org/10.1016/S0169-1368(99)00007-4

[33] Gupta, R.P. (2003) Remote Sensing Geology. Springer Berlin Heidelberg, Berlin, 655 pp. http://dx.doi.org/10.1007/978-3-662-05283-9

[34] Rowan, L.C. and Mars, J.C. (2003) Lithologic Mapping in the Mountain Pass, California Area Using Advanced Space-borne Thermal Emission and Reflection Radiometer (ASTER) Data. *Remote Sensing of Environment*, **84**, 350-366. http://dx.doi.org/10.1016/S0034-4257(02)00127-X

[35] Rowan, L.C., Hook, S.J., Abrams, M.J. and Mars, J.C. (2003) Mapping Hydrothermally Altered Rocks at Cuprite, Nevada Using Advanced Spaceborne Thermal Emission and Reflection Radiometer (ASTER), a New Satellite Imaging System. *Economic Geology*, **98**, 1019-1027.

[36] Ranjbar, H., Honarmand, M. and Moezifar, Z. (2004) Application of the Crosta Technique for Porphyry Copper Alteration Mapping Using ETM$^+$ Data in the Southern Part of the Iranian Volcanic Sedimentary Belt. *Journal of Asian Earth Sciences*, **24**, 237-243. http://dx.doi.org/10.1016/j.jseaes.2003.11.001

[37] Mars, J.C. and Rowan, L.C. (2006) Regional Mapping of Phyllic- and Argillic-Altered Rocks in the Zagros Magmatic arc, Iran, Using Advanced Spaceborne Thermal Emission and Reflection Radiometer (ASTER) Data and Logical Operator Algorithms. *Geosphere*, **2**, 161-186.

[38] Al Rawashdeh, S., Saleh, B. and Hamzah, M. (2006) The Use of Remote Sensing Technology in Geological Investigation and Mineral Detection in El Azraq-Jordan. *Cybergeo*: *European Journal of Geography*, 358.

[39] Gad, S. and Kusky, T. (2007) ASTER Spectral Ratioing for Lithological Mapping in the Arabian-Nubian Shield, the Neoproterozoic Wadi Kid Area, Sinai, Egypt. *Gondwana Research*, **11**, 326-335. http://dx.doi.org/10.1016/j.gr.2006.02.010

[40] Zhang, G.F., Shen, X.H., Zou, L.J., Li, C.J., Wang, Y.L. and Lu, S.L. (2007) Detection of Hydrocarbon Bearing Sand through Remote Sensing Techniques in the Western Slope Zone of Songliao Basin, China. *International Journal of Remote Sensing*, **28**, 1819-1833. http://dx.doi.org/10.1080/01431160600975329

[41] Rajesh, H.M. (2008) Mapping Proterozoic Unconformity-Related Uranium Deposits in the Rockhole Creek Area, Northern Territory, Australia Using Landsat ETM+. *Ore Geology Reviews*, **33**, 382-396. http://dx.doi.org/10.1016/j.oregeorev.2007.02.003

[42] Madani, A. and Emam, A. (2011) SWIR ASTER Band Ratios for Lithological Mapping and Mineral Exploration: A Case Study from El Hudi Area, South Eastern Desert, Egypt. *Arabian Journal of Geosciences*, **4**, 45-52. http://dx.doi.org/10.1007/s12517-009-0059-8

[43] Frei, M. and Jutz, S.L. (1989) Use of Thematic Mapper Data for the Detection of gold Bearing Formations in the Eastern Desert of Egypt. *Proceedings of the* 7*th Thematic Conference on Remote Sensing for Ore Exploration Geology II*, Calgary, 2-6 October 1989, 1157-1172.

[44] Visinescu, M., Stern, R.J. and Abdelsalam, M.G. (2000) Application of Remote Sensing Techniques in Gold Exploration in Wadi Allaqi Area, South-Eastern Desert, Egypt. Abstracts with Programs. *Geological Society of America*, **32**, 43.

[45] Singh, A. and Harrison, A. (1985) Standardized Principal Components. *International Journal of Remote Sensing*, **6**, 883-896. http://dx.doi.org/10.1080/01431168508948511

[46] Drury, S. (1993) Image Interpretation in Geology. 2nd Edition, Chapman and Hall, London.

[47] Kusky, T.M. and Ramadan, T.M. (2002) Structural Controls on Neoproterozoic Mineralization in the South Eastern Desert, Egypt: An Integrated Field, Landsat TM and SIR-C/X SAR Approach. *Journal of African Earth Science*, **35**, 107-121. http://dx.doi.org/10.1016/S0899-5362(02)00029-5

[48] Madani, A.A., Abdel Rahman, E., Fawzy, K.M. and Emam, A.A. (2003) Mapping of the Hydrothermal Alteration Zones at Haimur Gold Mine Area, South Eastern Desert, Egypt, Using Remote Sensing Techniques. *Egyptian Journal of Remote Sensing and Space Science*, **6**, 47-60.

[49] Gad, S.A. and Kusky, T.M. (2006) Lithological Mapping in the Eastern Desert of Egypt, the Barramiya Area, Using Landsat Thematic Mapper (TM). *Journal of African Earth Sciences*, **44**, 196-202. http://dx.doi.org/10.1016/j.jafrearsci.2005.10.014

[50] Sultan, M., Arvidson, R.E. and Sturchio, N.C. (1986) Mapping of Serpentinites in the Eastern Desert of Egypt Using Landsat Thematic Mapper Data. *Geology*, **14**, 995-999. http://dx.doi.org/10.1130/0091-7613(1986)14<995:MOSITE>2.0.CO;2

[51] Kaufman, H. (1988) Mineral Exploration along the Agaba-Levant Structure by Use of TM-Data Concepts, Processing and Results. *International Journal of Remote Sensing*, **9**, 1630-1658.

[52] Loughlin, W.P. (1991) Principal Component Analysis for Alteration Mapping. *Photogrammetric Engineering and Remote Sensing*, **57**, 1163-1169.

[53] Schmidt, K.J. (1991) Spectral Stratigraphy Applied to Analysis of Cretaceous Units at Como and Flat Top Anticlines, Southeast Wyoming. University of Wyoming, Laramie.

[54] Bennett, S.A., Atkinson, W.W. and Kruse, F.A. (1993) Use of Thematic Mapper Imagery to Identify Mineralization in the Santa Teresa District, Sonara, Mexico. *International Geology Review*, **35**, 1009-1029. http://dx.doi.org/10.1080/00206819309465572

[55] Martinetti, J.A., Duke, E.F. and Davenport, J.T. (1997) Comparison of Field-Based and Remote-Sensing Approaches Tomineral Exploration Models; Epithermal Quartz-Alunite-Gold Mineralization at Goldfield, Nevada. Abstracts with Programs—Geological Society of America 29, 6-50.

[56] Abdeen, M.M., Thurmond, A.K., Abdelsalam, M.G. and Stern, R.J. (2001) Application of ASTER Band-Ratio Images for Geologicalmapping in Arid Regions; the Neoproterozoic Allaqi Suture, Egypt. *Geological Society of America*, 2001 *Annual Meeting*, Abstracts with Programs—Geological Society of America, **33**, 289.

[57] Kang, K.K., Song, K.Y., Ahn, C.H. and Won, J.S. (2001) Reflectance of Geological Media by Using a Field Spectrometer in the Ungsang Area, Kyungsang Basin. *Korean Journal of Remote Sensing*, **17**, 165-181.

[58] Tangestani, M.H. and Moore, F. (2002) Porphyry Copper Alteration Mapping in the Meiduk Area, Iran. *International Journal of Remote Sensing*, **23**, 4815-4825. http://dx.doi.org/10.1080/01431160110115564

[59] Volesky, J.C., Stern, R.J. and Johnson, P.R. (2003) Geological Control of Massive Sulfide Mineralization in the Neoproterozoic Wadi Bidah Shear Zone, Southwestern Saudi Arabia, Inferences from Orbital Remote Sensing and Field Studies. *Precambrian Research*, **123**, 235-247. http://dx.doi.org/10.1016/S0301-9268(03)00070-6

[60] Aydal, D., Arda, E. and Dumanlilar, Ö. (2007) Application of the Crosta Technique for Alteration Mapping of Granitoidic Rocks Using ETM+ Data: Case Study from Eastern Tauride Belt (SE Turkey). *International Journal of Remote Sensing*, **28**, 3895-3913. http://dx.doi.org/10.1080/01431160601105926

[61] Kargi, H. (2007) Principal Components Analysis for Borate Mapping. *International Journal of Remote Sensing*, **28**, 1805-1817. http://dx.doi.org/10.1080/01431160600905003

[62] Thornton, C.P. and Tuttle, O.F. (1960) Chemistry of Igneous Rocks, [Part] 1. Distribution Index. *American Journal of Science*, **258**, 664-684. http://dx.doi.org/10.2475/ajs.258.9.664

[63] Pearce, J.A. (1983) Role of the Sub-Continental Lithosphere in Magma Genesis at Active Continental Margin. In: Hawkesworth, C.J. and Norry, M.J., Eds., *Continental Basalts and Mantle Element Xenoliths*, Shiva Publishing Ltd., Cambridge, Mass., 272 p.

[64] Cox, K.G., Bell, J.D. and Pankhurst, R.J. (1979) The Interpretation of Igneous Rocks. George Allen and Unwin, London.

[65] Winchester, J.A. and Floyd, P.A. (1977) Geochemical Discrimination of Different Magma Series and Their Differentiation Products Using Immobile Elements. *Chemical Geology*, **20**, 325-343. http://dx.doi.org/10.1016/0009-2541(77)90057-2

[66] MacDonald, G.A. (1968) Composition and Origin of Hawaii Lavas. *Geological Society of America Memoirs*, **116**, 477-522. http://dx.doi.org/10.1130/MEM116-p477

[67] Irvine, T.N. and Baragar, W.R.A. (1971) A Guide to the Chemical Classification of the Common Volcanic Rocks. *Canadian Journal of Earth Sciences*, **8**, 523-548. http://dx.doi.org/10.1139/e71-055

[68] Miyashiro, A. (1975) Volcanic Rock Series and Tectonic Setting. *Annual Review of Earth and planetary Sciences*, **3**, 251-269. http://dx.doi.org/10.1146/annurev.ea.03.050175.001343

[69] Pearce, J.A., Lippard, S.J. and Roberts, S. (1984) Characteristics and Tectonic Significance of Supra-Subduction Zone Ophiolite. In: Kokelaar, B.P. and Howells, M.F., Eds., *Marginal Basin Geology*, In: *Geological Society*, *London*, *Special Publications*, Vol. 16, Blackwell Scientific Publications, Oxford, 77-94.

[70] Wood, D.A. (1980) The Application of the Th-Hf-Ta Diagram to Problems of Tectonomagmatic Classification and Establishing the Nature of Crustal Contamination of Basaltic Lava of the British Tertiary Volcanic Province. *Earth and Planetary Science Letters*, **50**, 11-30. http://dx.doi.org/10.1016/0012-821X(80)90116-8

[71] Stern, R.J. and Hedge, C.E. (1985) Geochronologic and Isotopic Constraints on Late Precambrian Crustal Evolution in the Eastern Desert of Egypt. *American Journal Science*, **285**, 97-127. http://dx.doi.org/10.2475/ajs.285.2.97

[72] Bentor, Y.K. and Eyal, M. (1987) The Geology of Southern Sinai, Its Implication for the Evolution of the Arabian-Nubian Massif Volume 1: Jebel Sabbagh Sheet. Israel Academy of Sciences and Humanities, Jerusalem, 484 p.

[73] Stern, R.J. and Gottfried, D. (1986) Petrogenesis of Late Precambrian (575-600 Ma) Bimodal Suite in Northeast Africa. *Contributions to Mineralogy and Petrology*, **92**, 492-501. http://dx.doi.org/10.1007/BF00374431

[74] Garfunkel, Z. (2000) History and Paleogeography during the Pan-African Orogen to Stable Platform Transition: Reappraisal of the Evidence from Elat Area and the Northern Arabian-Nubian Shield. *Israel Journal of Earth Sciences*, **48**, 135-157.

[75] Genna, A., Nehlig, P., Le Goff, E., Guerrot, C. and Shanti, M. (2002) Proterozoic Tectonism of the Arabian Shield. *Precambrian Research*, **117**, 21-40. http://dx.doi.org/10.1016/S0301-9268(02)00061-X

[76] Eby, G.N. (1992) Chemical Subdivision of the A-Type Granitoids: Petrogenetic and Tectonic Implications. *Geology*, **20**, 641-644. http://dx.doi.org/10.1130/0091-7613(1992)020<0641:CSOTAT>2.3.CO;2

[77] Pearce, J.A. and Norry, M.J. (1979) Petrogenetic Implications of Ti, Zr, Y, and Nb Variation in Volcanic Rocks. *Contributions to Mineralogy and Petrology*, **69**, 33-47. http://dx.doi.org/10.1007/BF00375192

[78] Pearce, J.A. (1980) Geochemical Evolution for the Genesis and Eruptive Setting of Lavas from Tethyan Ophiolites. In: Panayiotou, A., Ed., *Opiolites*, Geological Survey Department, Cyprus, 261-272.